ADVANCED MATERIALS TECHNOLOGIES
www.advmattechnol.de

Design and Analysis of a 3D Frictional Mechanical Metamaterial for Efficient Energy Dissipation

*Eunhyeuk Jeong, Emilio Calius, and Maziar Ramezani**

This study introduces a novel frictional mechanical metamaterial composed of a central hexagon or re-entrant honeycomb frame, a lower section with four tapered columns, and an upper portion with a blade shape. When subjected to an external uniaxial force, the 3D structure of the metamaterial utilizes sliding interactions to dissipate frictional energy. The mechanical properties of the proposed metamaterial, such as load-displacement relationships, hysteresis area, and peak force, can be fine-tuned by adjusting geometric parameters and constituent materials. Extensive analysis is conducted through experimental compression tests, finite element (FE) simulations, and theoretical modeling. Comparative assessments of the metamaterial's energy dissipation performance demonstrated a good agreement between experimental and simulation results, with minor variations observed for deeper compression cycles. The proposed metamaterial offers the potential for superior elastic energy absorption and dissipation, making it a promising solution for applications requiring repeated energy dissipation or damping under cyclical loads while maintaining a lightweight profile.

1. Introduction

Various geometric designs can produce different levels of energy dissipation and absorption to mitigate external shocks and protect the core components of machines, buildings, and even human beings. Energy dissipation structures, including dampers,[1–3] and anti-seismic buildings,[4,5] are essential, particularly in regions located on tectonic plate boundaries. In industries like aerospace and automotive, the need for effective braking systems and energy dissipation is paramount to ensure the safety of passengers and crucial components during impact events.[6–8] Structures designed for efficient energy absorption and dissipation play a vital role in protecting lives and valuable assets from unforeseen impacts.

To enhance the performance of energy dissipation and absorption, researchers have consistently explored unique geometric structures, drawing inspiration from both human intuition and nature's intricate designs, such as the beetle forewing,[9] woodpecker's beak,[10] and the mesocarp layer of a pomelo fruit.[11] The pursuit of novel geometry has led to increased structural complexity, making the manufacture of prototype specimens challenging. However, since Chuck Hull's invention of the 3D printer in 1983,[12] continuous advancements have made it possible to create objects with complex shapes that were once considered unattainable.

Metamaterials, characterized by unique properties not found in natural monolithic materials,[13] have opened up new avenues in various fields, including negative Poisson's ratio,[14,15] cloaking,[16,17] and high energy absorption.[18] In 1968 Veselago was the first to analyze the interesting theoretical effects that would arise when an electromagnetic wave propagated through a material with both negative permeability and positive permittivity.[19,20] John B. Pendry looked for workable ways to develop left-handed materials (LHM), also known as negative-index materials, in 1999 that deviated from the conventional right-hand rule. In order to depict the flow of wave propagation energy, LHM creates a relationship between the wave propagation vector and the Poynting vector.[21] Their groundbreaking work laid the foundation for manipulating electromagnetic waves in unprecedented ways, leading to applications ranging from cloaking devices to super lenses. Similarly, Leonhardt's contributions, proposing optical transformation techniques to manipulate wave propagation using metamaterials, opened new avenues for controlling light at the nanoscale, inspiring a wave of research into metamaterial-based devices with extraordinary capabilities.[22] Over the past two decades, engineers have created various metamaterials with applications in acoustics, thermodynamics, electromagnetics, and mechanics, leading to innovations like invisibility cloaks and superior energy absorbers.

Multiple methods for absorbing and dissipating mechanical energy through metamaterials have been explored. Prototypes in the form of lattice struts, for instance, achieve substantial

E. Jeong, E. Calius, M. Ramezani
Department of Mechanical Engineering
Auckland University of Technology
Auckland 1010, New Zealand
E-mail: maziar.ramezani@aut.ac.nz

The ORCID identification number(s) for the author(s) of this article can be found under https://doi.org/10.1002/admt.202400614

[Correction added on August 8, 2025, after online publication: The copyright line for this article was changed in this version]

DOI: 10.1002/admt.202400614

energy absorption by deforming and breaking the internal lattice structure upon external impact.[23] Sandwich panels, with enhanced lattice structures in the center, aim to exploit the plastic deformation of the lattice.[24] Origami or kirigami patterns applied to metamaterial geometry enable directional fracture, optimizing energy absorption.[25] However, these methods often result in irreversible processes and cannot be reused after energy-dissipating operations.

The need for reversibility, that is, reusability, together with high energy absorption has led to several novel concepts being proposed over the last 5 years. One approach involves granular metamaterials with reversible hysteresis, combining rigid cylinders with flexible, stretchable elements. This novel metamaterial maintains structural integrity through stretchable elements while dissipating frictional energy during cylinder sliding, akin to bistable metamaterials.[26] Another concept based on frictional energy dissipation employs a honeycomb structure, where each cell contains a frictional mechanism that consists of beams whose tips slide along an inclined surface when the honeycomb cell undergoes in-plane compression.[27] This metamaterial generates a significant hysteresis area and the proposed 2D structure can be expanded into 3D to further improve performance.

Multistable metamaterials that can switch between multiple stable states due to their reversibility dissipate energy when changing states and offer reusability within the range of elastic deformation.[28] One limitation is that they require additional manual intervention to return to their original state. Yet another concept that has been proposed is that of "intertwined structures". This metamaterial consists of three key components: a soft elastomer, a stiff frame, and steel rods, interacting to absorb energy as rods pass into elastomer holes when subjected to external force.[29] More recently, energy-absorbing metamaterials with multilayered chiral topologies have been presented. The energy dissipation occurring at the interface between adjacent discs comprising the metamaterial enables the metamaterial to self-repair, making it reusable.[30] In addition, it has been demonstrated that mechanical metamaterials with negative Poisson's ratios, known as auxetics, provide benefits in impact protection[31] and improved fracture resistance.[32] However, a metamaterial combining the concept of friction with the re-entrant structure topology, which is one of those that exhibit a negative Poisson's ratio, has not yet been investigated.

Here we present a new reusable 3D frictional metamaterial unit cell in which multiple pillars slide along curved surfaces when an external force compresses the unit cell, inducing friction and enhanced energy dissipation density. This proposed concept is different from conventional shock absorbers, which focus on energy absorption at high strain rates. Both auxetic and non-auxetic versions of this unit cell are formulated. A theoretical model and a FE analysis methodology are developed to analyze the unit cell's load-displacement response and derive its energy dissipation. To demonstrate the supposed new design concept of metamaterials, we validated the conventional hexagonal single-unit cell geometry by comparing FE simulation with experiments and then presented several simple arrangements of this unit cell. The conventional and auxetic versions of the unit cell are fabricated by a polymeric additive manufacturing process and demonstrate experimentally that the predicted performance can be achieved under various levels of compression. These designed structures are intended to work at small strain regime to avoid plastic deformation. In addition, there is no consideration of lubrication to maximize energy dissipation through friction. Interestingly, it is found that the experimentally measured performance is somewhat better than predicted and that the auxetic unit cells dissipate only a little more energy. The FE simulation methodology is then applied to assemblies with different numbers of unit cells, that is, finite metamaterials. This analysis indicates that only a moderate number of such cells is needed to estimate the performance of larger frictional metamaterial domains.

2. Experimental Section

2.1. Design of the Unit Cell

The proposed unit cell is composed of three distinct parts: a hexagonal elastic frame, either classic honeycomb (**Figure 1**g–i) or re-entrant (**Figure 2**a–c), the upper blade-like structure (Figure 1d–f) and four tapered pillars or columns (Figure 1a–c) in the lower one. This blade and column structure forms four pairs of contact surfaces to generate friction with the frame sidewalls acting akin to springs, storing energy through deformation upon loading and releasing it during unloading. It is important to note that this unit cell is intended to operate within the elastic range to ensure reusability. The presented columns design was finalized after a significant design development and optimization process. Various design concepts and improvements to their performance were investigated to determine the shape of the proposed columns. The blades and columns were designed to maximize the contact surface area within a volume. The cross-sectional area of the four columns progressively reduces from the base to the top, with a cross-sectional shape that combines a quarter circle and a quarter circular spandrel. The blade shape matches the surface profile of the columns, and upon external loading comes into contact and then slides along the column to convert mechanical energy into heat. The detailed dimensions of each part of the unit cell are listed in **Table 1**.

The unit cell was designed to be manufactured in three separate 3D printed parts and assembled to form a complete unit cell, as discussed in the next section. This approach allowed the gap between contact surfaces to be effectively set to practically zero, thereby achieving energy dissipation as soon as an external force is applied. This design also provides modularity, allowing different part combinations to be mixed and matched together and parts to be replaced when necessary.

2.2. Material and Fabrication

All unit cell parts were 3D printed by fused deposition modeling (FDM) using a Caribou MK3S 320 with Filamentum CPE HG100 as the constituent material. CPE (Co-Polyester), also known as Polyethylene Terephthalate, stands out as a robust and durable filament that is characterized by robust interlayer adhesion. The 3D printer's nozzle temperature was set to 270 °C and the bed temperature to 80 °C, in accordance with the filament supplier's recommendations. The infill value was set to 50% to balance manufacturing time, material usage, and mechanical strength of the printed parts.

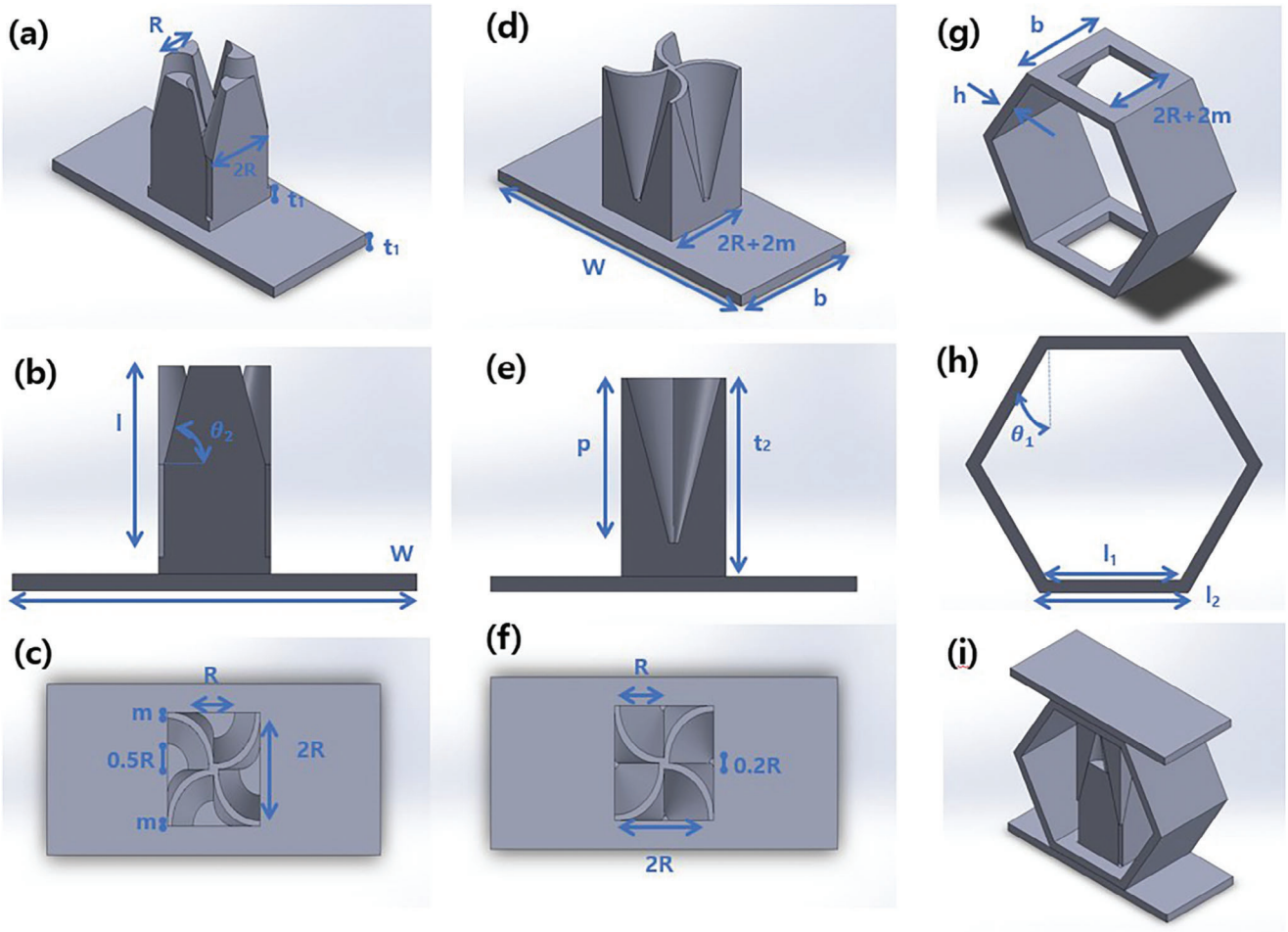

Figure 1. Various views (a–c) of the four columns part, (d–f) of the four-blade part, and (g,h) of the conventional hexagonal frame, and (i) complete unit cell appearance after assembling.

As shown in Figures 1g and 2a, the hexagonal frame has rectangular openings in its upper and lower base sides that are required for assembly. This necessitated the addition of support during printing. Scarring from support removal was minimized by selecting the support material style as "Snug", which also conserved filament. Given the nature of the FDM process, the strength of the resulting structures will vary depending on the direction of external loading relative to the orientation of the filaments and layers from which the part is constructed. To enhance the strength of the unit cell's frame under vertical forces, this part was manufactured such that the hexagonal shape was in the printer bed plane and filament ran along the perimeter of the hexagon.

Once all three parts had been 3D printed, the unit cells were manually assembled by pushing the upper blade and lower columns through the openings in the frame until they came into contact, resulting in four of each of the test articles illustrated in **Figure 3**.

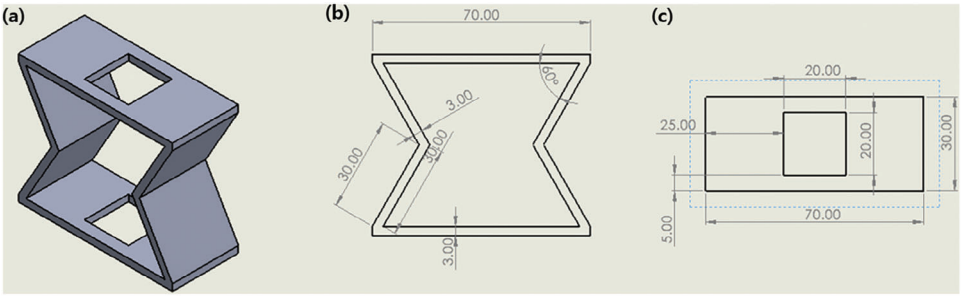

Figure 2. (a) Isometric view of the re-entrant hexagonal frame, (b) front view, and (c) top view.

Table 1. The main dimensions of the hexagonal unit cell are illustrated in Figure 1.

Dimensions of the unit cell												
b (mm)	h (mm)	Θ_1 (deg)	l_1 (mm)	l_2 (mm)	R (mm)	Θ_2 (deg)	l (mm)	p (mm)	t_1 (mm)	t_2 (mm)	m (mm)	W (mm)
30	3	30	30	33.46	9	75.58	34	31.5	3	38	1	70

To characterize the as-printed compression properties of CPE HG100, five cylindrical test specimens were printed in addition to the unit cell test article parts. These cylindrical specimens had a diameter that was equal to its height of 20 mm (Appendix SA, Supporting Information). And to characterize its frictional properties, two kinds of rectangular block specimens were also printed.

2.3. Theoretical Model

For the model proposed in this study, the work done not only by sliding friction of internal contact surfaces but also by the elastic deformation of the contact surface support structure and hexagonal frame should be taken into account for calculating total work when the proposed unit cell is compressed as shown in Figure 5.[27] That the total work is a sum follows from the additive property of the dot product in the expression defining work in mechanical systems.[33]

$$W_{novel} = \int \vec{F} \bullet d\vec{r} = \int \left(\vec{F}_{honeycomb} + \vec{F}_{bending} + \vec{F}_{sliding}\right) \bullet d\vec{r}$$
$$= \int \vec{F}_{honeycomb} \bullet d\vec{r} + \int \vec{F}_{bending} \bullet d\vec{r} + \int \vec{F}_{sliding} \bullet d\vec{r} \quad (1)$$

Therefore, a simpler representation of the total work of the proposed frictional mechanical metamaterial is:

$$W_{novel} = W_{honeycomb} + W_{bending} + W_{sliding} \quad (2)$$

where $W_{honeycomb} = \int \vec{F}_{honeycomb} \bullet d\vec{r}$, $W_{bending} = \int \vec{F}_{bending} \bullet d\vec{r}$, and $W_{sliding} = \int \vec{F}_{sliding} \bullet d\vec{r}$

Based on the slow loading rate applied in our experiments (3 mm min^{-1}), it is reasonable to assume that the friction is not generating enough heat to create a significant temperature difference between the contact surfaces and the rest of the structure, and therefore the heat flow is small enough to be negligible. Therefore, the total energy absorbed in the metamaterial unit cell is the sum of the work done in all the elastic deformations and frictional sliding. The following formulations of expressions for each of these work terms in Equation (2) are based on simplifying assumption that may not capture the full complexity of the kinematics of the frame, blades, and columns, but they provide a simple approach to estimating the total mechanical energy absorbed by the unit cell during the compression loading phase.

A honeycomb unit cell with a geometry similar to that of the hexagonal frame in the proposed frictional metamaterial unit cell had been studied by Gibson.[34] When the honeycomb cell deformation under load is dominated by sidewall bending, the applied displacement δ can be calculated by Equation (3).

$$\delta = \frac{F \times L^3 \times \sin\left(\theta_1\right)}{12 \times E \times I_{honeycomb}} \quad (3)$$

where F is the applied external force on the unit cell, E is the Young's Modulus of the constituent material, θ_1 is the angle between the unit cell's sidewall and the longitudinal axis. (Figure 1h) and $I_{honeycomb}$ is the moment of inertia of the frame sidewall's rectangular cross-section.

$$I_{honeycomb} = \frac{b \times h^3}{12} \quad (4)$$

Here, b is the extruded length of the unit cell and h is the wall thickness of the unit cell. The side wall length L is defined as:

$$L = \frac{l_1 + l_2}{2} \quad (5)$$

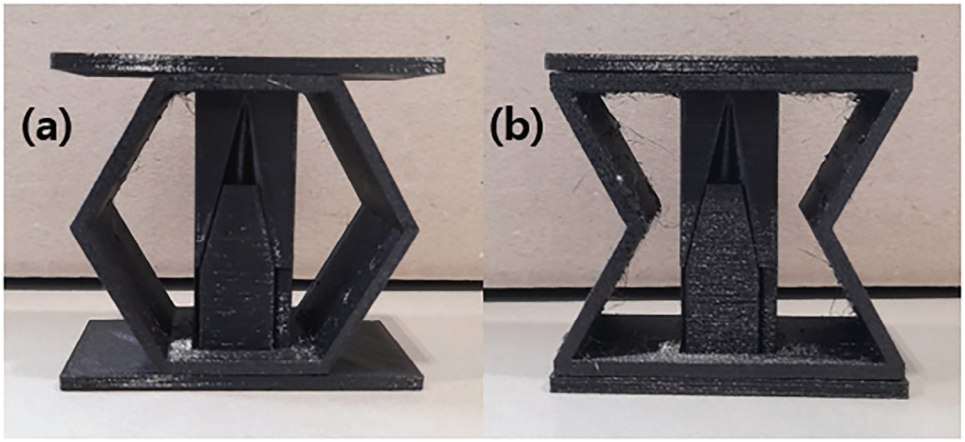

Figure 3. Unit cells are additively manufactured by FDM with (a) a conventional hexagonal frame and (b) a re-entrant frame.

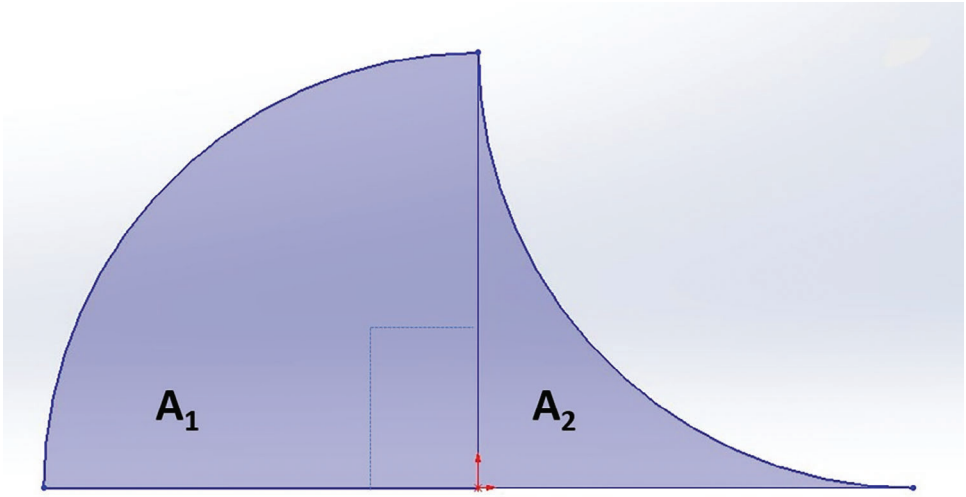

Figure 4. Cross-section of each column is divided into two areas. A_1 is the quarter circle part and A_2 is the quarter circular spandrel part.

where l_1 and l_2 are the inner and outer side lengths respectively. The applied force required to obtain a certain displacement can then be calculated by substituting for $I_{honeycomb}$ and L and rearranging Equation (3).

$$F = \frac{E \times b \times h^3 \times \delta}{L^3 \times sin^2\left(\theta_1\right)} \tag{6}$$

Then the work of a cell deformation can be calculated by multiplying the force by deflection as below:

$$W_{honeycomb} = \int_0^{\delta} F\, d\, \delta' = \frac{E \times b \times h^3 \times \delta^2}{L^3 \times \sin^2\left(\theta_1\right) \times 2} \tag{7}$$

The four internal vertical columns can be split into two parts – the same cross-section area part from the base to the around intermediate section part and a not uniform cross-section area part from the middle section to the top of the columns. The part directly related to bending is the column part with a uniform cross-sectional area, so the deflection of each of the columns on the base of the unit cell due to bending can be expressed as Equation (8):[35]

$$\delta_{bending} = \frac{F_{bending} \times l^3}{3 \times E \times I_{column}} \tag{8}$$

where $F_{bending}$ is the force applied at the free end of the column and l is the length of the column.

The cross-sectional shape of each column for friction can be divided into two parts, a quarter circle and a quarter circular spandrel (**Figure 4**), each of which has a different equation to calculate the moment of inertia. Therefore, the moment of each part should be calculated separately, and the use parallel axis theorem to calculate the whole moment of inertia.

The moment of inertia of each part concerning the X' axis can be denoted as:[36]

$$I_{columnX} = \sum \left(I + Ad^2\right) = I_1 + A_1 d_{y1}^2 + I_2 + A_2 d_{y2}^2 \tag{9}$$

Same way, the moment of inertia of each part with respect to the Y' axis can be expressed as:

$$I_{columnY} = \sum \left(I + Ad^2\right) = I_1 + A_1 d_{x1}^2 + I_2 + A_2 d_{x2}^2 \tag{10}$$

The columns are not directly constrained by explicit boundary conditions but are instead influenced by the overall boundary conditions of the hexagonal unit cell. This approach ensures that the internal interactions and deformations of the columns reflect the realistic loading conditions applied to the entire unit cell.

The maximum moment of inertia I_{column} is selected to maximize the bending force ($F_{bending}$) and then Equation (8) can be rearranged and when multiplied by the deflection gives the work of the bending force as:

$$W_{bending} = \int_0^{\delta} F_{bending}\, d\delta' \times 4 = \frac{\delta_{bending}^2 \times 3 \times E \times I_{column}}{2 \times l^3} \times 4 \tag{11}$$

The multiplication by 4 at the back reflects the presence of 4 tapered columns inside the unit cell. The amount of work by sliding, also known as frictional energy dissipation, can be calculated by multiplying the normal force on the contact surface by the coefficient of friction (μ) and the sliding distance ($\delta_{sliding}$):

$$W_{sliding} = \mu \times N \times \delta_{sliding} \tag{12}$$

The normal force N on the contact surfaces and the sliding distance can be expressed as:

$$N = \frac{F_{bending}}{cos\left(\theta_2\right)} \tag{13}$$

$$\delta_{sliding} = \frac{\delta}{sin\left(\theta_2\right)} \tag{14}$$

Table 2. Comparison of energy dissipation between theoretical model, FE simulations, and experiments.

Max effective strain (mm/mm)	Theoretical (Sliding friction only)	Theoretical (Total work)	FE simulation (Conventional)	Experimental (Conventional)		FE simulation (Re-entrant)	Experimental (Re-entrant)	
				Min	Max		Min	Max
0.0156	44.23	61.16	64.98	58.99	59.80	68.81	67.32	73.45
0.0312	176.93	244.64	276.86	288.23	319.98	293.03	319.30	354.37
0.0467	398.10	550.44	632.99	624.43	773.65	669.02	627.12	756.71

Bending displacement can be obtained from the applied displacement δ (Equation (3)):

$$\delta_{bending} = \frac{\delta}{tan\left(\theta_2\right)} \tag{15}$$

Substituting Equations (11,13–15) into Equation (12) the work is arrived at through sliding:

$$W_{sliding} = \frac{\mu \times 3 \times E \times I_{Column} \times \delta^2}{l^3 \times cos\left(\theta_2\right) \times sin\left(\theta_2\right) \times tan\left(\theta_2\right)} \times 4 \tag{16}$$

The multiplication by 4 at the back reflects the presence of 4 pairs of contact surfaces from the four columns. The proposed new unit cell consists of a hexagonal frame with four inner columns for sliding friction and bending. Therefore, the total work quantity would be denoted as:

$$W_{novel} = \frac{E \times b \times h^3 \times \delta^2}{L^3 \times sin^2\left(\theta_1\right) \times 2} + \frac{\delta_{bending}^2 \times 6 \times E \times I_{column}}{l^3} + \frac{\mu \times 3 \times E \times I_{column} \times \delta^2 \times 4}{l^3 \times cos\left(\theta_2\right) \times sin\left(\theta_2\right) \times tan\left(\theta_2\right)} \tag{17}$$

Equation (17) includes all three factors – $W_{honeycomb}$, $W_{bending}$, and $W_{sliding}$ – indicates the energy absorption of the unit cell. The $W_{honeycomb}$ and $W_{bending}$ are related to elastic energy storage, while the $W_{sliding}$, referring to frictional sliding, which contributes directly to energy dissipation. The energy dissipation of the proposed structure was calculated using only $W_{sliding}$, as well as the overall energy absorption capacity by adding all three terms of work presented in Equation (17). These theoretical results are compared with the hysteresis loop areas obtained from the experiments and FE models (Figure 10 and **Table 2**).

2.4. FE Simulations

FE simulations of the unit cell under compression were conducted using ANSYS Workbench 2023 R2. It was assumed that the unit cell was operating within the material's elastic range and that the material was linear elastic. The material properties used in the simulations were derived from the compression tests with cylindrical specimens and the coefficient of friction tests. Table S1 in the Appendix (Supporting Information) describes the measured CPE HG100 material properties that were used in the FE analysis.

Quadratic element order is selected to correspond to complex geometries and bending deformations. The solid part and contact area of the model possess SOLID187 and CONTA174 elements, respectively. SOLID187 is defined by 10 nodes having three degrees of freedom at each node. CONTA174 is selected to describe contact and sliding between 3D target surfaces. As boundary conditions to perform the simulation, the bottom surface of the unit cell had been applied to the fixed support and the top surface had been selected to apply displacement condition.

When assembling the three parts that compose the unit cell, the contacts between the hexagonal frame structure and the other two parts were defined as bonded contacts. This choice reflects the tight fit between the frame and these other two parts that prevented them from separating or sliding against each other. In contrast, the contact surface pairs between the upper part with its blade structure and the bottom part with its four columns were configured as frictional contact. Symmetric contact behavior was specified since both sides were made of the same material, curved shapes that both possess the same proportion of angles, obviating the need to distinguish between contact and target surfaces.

The mesh quality on these frictional contact surfaces plays a crucial role in capturing accurate results related to energy dissipation. However, it is essential to strike a balance between accuracy and computational efficiency, as finer meshes come at the cost of increased memory usage and longer solve times. To find this balance, a mesh convergence study was conducted by varying the contact sizing resolution values within ANSYS Workbench (Appendix SB, Supporting Information).

Given the challenges in achieving a mesh convergence solution, the augmented Lagrange formulation was selected to address contact formation. Additionally, large deformation and the unsymmetric Newton–Raphson solver option were enabled to account for significant displacement and relatively high coefficients of friction.

2.5. Compression Tests

Both the unit cell and material characterization specimens underwent quasi-static compression testing in a Tinius Olsen H10K-S universal testing machine (Serial No.0162) with a Hounsfield 10KN load cell (Serial No.703053). The tests were conducted under displacement control at room temperature, without any heating or cooling, using a compression speed of 3 mm min^{-1}. Each unit cell test was repeated three or four times under three distinct displacement conditions: 1, 2, and 3 mm. **Figure** 5a shows an abstract depiction of applying compression to a unit cell model, while Figure 5b captures the actual compression experimental setup.

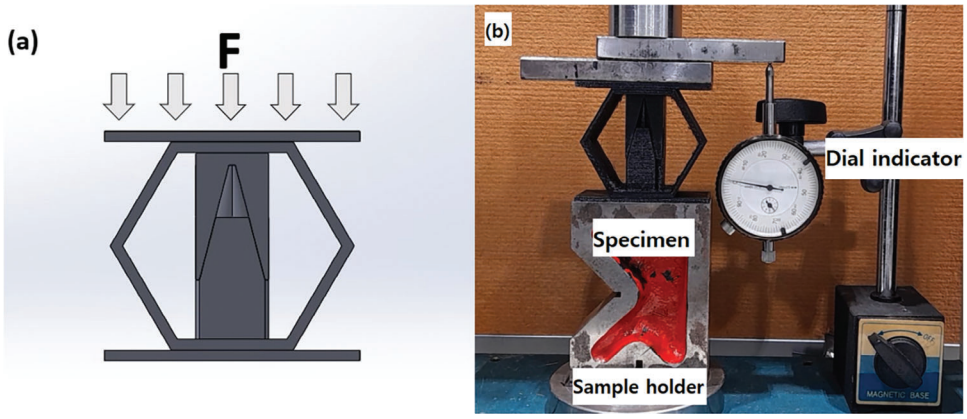

Figure 5. (a) Schematic diagram for describing the compressive load applied to the unit cell and (b) image of the uniaxial compression test setup.

2.6. Coefficient of Friction Measurement

The Coefficient of Friction (COF) between the two 3D-printed CPE HG100 surfaces was measured with a linear reciprocating tribometer (DUCOM, model: TR-282) using a pin-on-plate set up with a 6 mm diameter pin. The tests were conducted under 30 N applied load and 2 Hz sliding frequency for 30 min at room temperature (22 °C) and under dry contact condition. Winducom software was used for recording the frictional forces and the COF. The test samples exhibited good wear resistance and a consistently stable COF was obtained.

2.7. Scaling from Unit Cell to Metamaterial

The proposed hexagonal unit cell is intended to be used as a building block from which to construct energy-dissipating metamaterials. Therefore, several finite metamaterials were assembled from the unit cells described in Section 2.1 to evaluate the influence of the change in boundary conditions and the interactions between unit cells. These metamaterials' energy dissipation performance was analyzed through FE simulations that made use of the experimentally verified FE model of the unit cell. Because of the computational cost only a limited number of unit cells were considered, and the investigation focused on the trend in energy dissipation as the number of units increased. The load-displacement cycles and energy dissipation of these metamaterials were compared to that of a single unit cell subjected to the same compression cycle, with a peak effective strain of under 4.67%.

Metamaterials consisting of 8- and 13-unit cells were assembled into structures with the same height, but different widths as shown in **Figure 6**b,d. In order to achieve the same peak effective strain during the compression cycle, a total vertical compression of 1.5 mm was applied because the maximum height of the assembly is three times that of a single unit cell. To assess the sensitivity of its performance to the height-to-width ratio, an 11-unit cell model with 4 rows was also modeled, as shown in Figure 6c. A higher vertical compression of 2 mm was applied to this taller structure to achieve the same effective strain. These three assemblies represent steps in the transition from single unit cell to metamaterial and provide insight into the relative influence of scale effects on performance. These proposed assembled geometries are just sample arrangements of multiple unit cells to investigate and present the performance and behavior of the proposed design, and the proof of concept that the proposed frictional metamaterial offers effective energy dissipation. Due to the computational resource constraints, the number of unit cells composing the multi-unit cell structures was minimized in the FE simulation.

In order to more efficiently study the performance of periodic systems consisting of numerous unit cells a representative volume element (RVE) was defined as shown in **Figure 7**, to which periodic boundary conditions (PBCs) were then applied. Unlike the single-wall-thick hexagonal unit cell used in previous FEA simulations, in this RVE the frame sides are twice as thick as the thickness of a single unit cell hexagonal frame, except for the top and bottom sides. A single hexagonal frame is assumed to be located in the center of a structure made up of countless hexagons, the applied displacement boundary conditions are changed such that the top and bottom faces are subjected to half of the total displacement, directed toward the center of the unit cell on each side, for both RVE and unit cell. This allows horizontal motion to occur as they are no longer fixed in the test machine. Appropriate constraint equations set up to represent the PBCs are listed in Table S4 in Appendix SD (Supporting Information).

3. Results

Figure 8a–c illustrates the deformed and undeformed forms of the proposed unit cell. Figure 8a shows the situation immediately after the end of the unloading step of the unit cell, Figure 8b depicts the deformed unit cell in the vertical direction (y-axis) immediately after the end of the loading step, and Figure 8c displays the deformed unit cell in the lateral direction (x-axis) immediately after the end of the loading step. To explicitly represent the deforming shape, an x3.2 scale factor has been applied. It is notable in Figure 8a that the displacements of the columns inside the unit cell do not return to zero completely at the end of unloading. In the case of Figure 8b, the displacement is expressed as a negative value because the direction of the external force from the top of the unit cell downward is opposite to the y-axis of the coordinate system. For Figure 8c, the displacement values are represented as positive for the left side and negative for the right side because

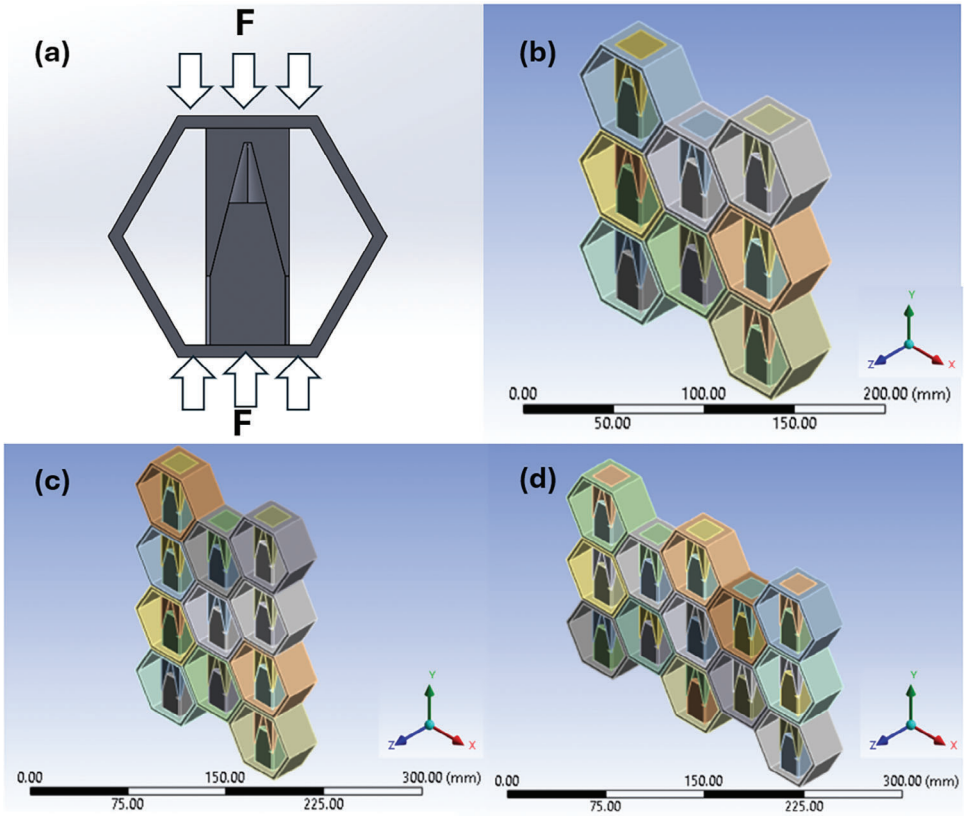

Figure 6. (a) Schematic diagram illustrating the external compression applied on a single unit cell, and finite metamaterials with (b) eight unit cells, (c) eleven unit cells and (d) thirteen unit cells. Note that in these simulations the wide loading plate parts at the top and bottom of the unit cell model was not present.

the direction of lateral displacement of the left and right sides is opposite to each other. Both Figure 8b,c show the deformation for a displacement of 3 mm from the top of the unit cell to the bottom (in the direction of the negative y-axis), which is somewhat exaggerated due to the auto-scale factor of 2.

The frictional stress contour plot on the contact surfaces of the geometry in the FE simulations is also generated as a typical example to show a stress distribution. One of the contact surfaces located on the four columns is point-symmetric through the center point of the unit cell and therefore exhibits the same frictional stress distribution for every column. The result indicates that significant stress concentrations are present at the bottom edges of these contact surfaces at the end of the loading step (**Figure 9**).

The graphs in **Figure 10**a–c depict the hysteresis loops obtained from experiments with maximum vertical compression displacements of 1, 2, and 3 mm, respectively, and the FE simulations of these load cycles for the conventional hexagonal unit cell. When the conventional hexagonal frame is replaced with a re-entrant frame, the resulting experimental and simulated hysteresis loops under the same load cycles are plotted in Figure 10d–f. These cycles are expressed in terms of effective stress and strain in Figure 10 as the unit cell is intended to be the building block

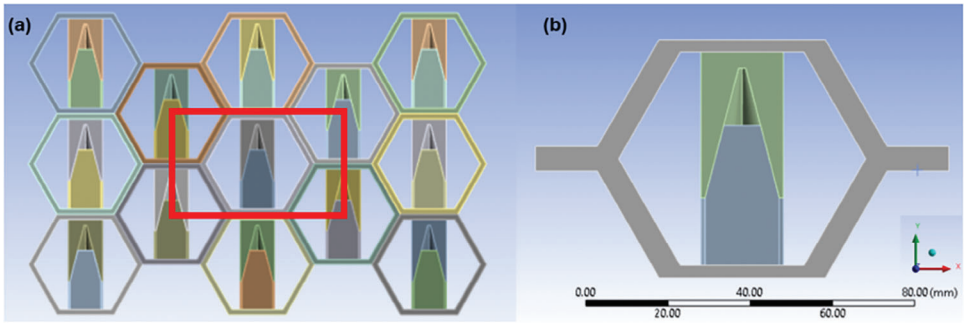

Figure 7. a) RVE in a honeycomb structure with internal structures for sliding (Rectangular area in red). b) Front view of RVE. The internal structures in the four corners of the red rectangle from the red rectangular have been removed, as sliding is not expected with only partial bodies.

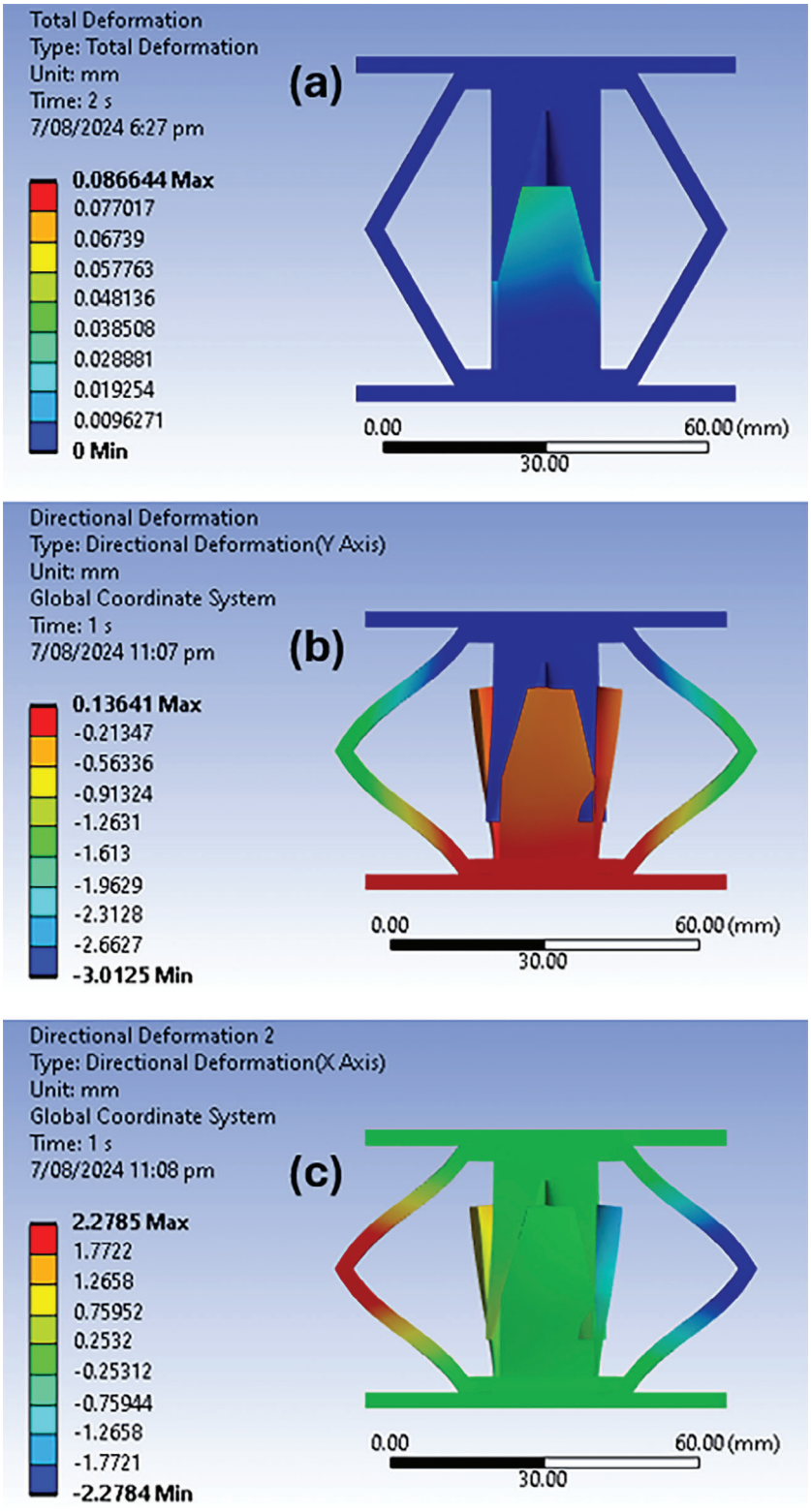

Figure 8. Displacement contour plots for the unit cell in three states: (a) total deformation at the end of the unloading step, (b) vertical deformation at the end of the loading step, (c) horizontal deformation at the end of the loading step. These deformations have been scaled up to more clearly show the deformed shape. These profiles are extracted from the FE simulation for an applied compressive displacement of 3 mm (see curve labeled FEA 3 in Figure 10c).

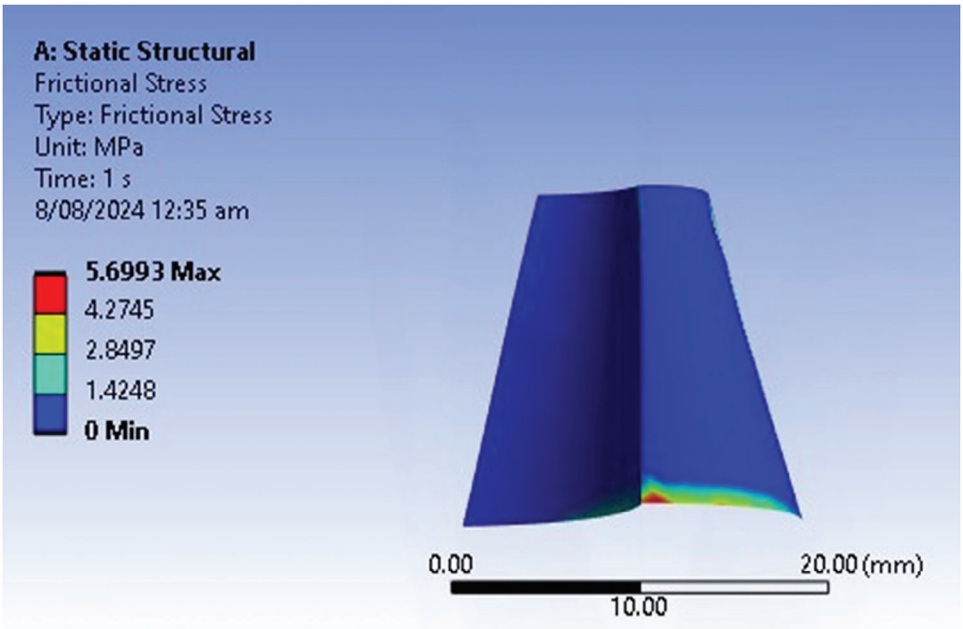

Figure 9. Frictional stress distribution on the one of the four identical contact surfaces of the unit cell model at the end of the loading step for the same compression condition as shown in Figure 8.

of an architected material. The effective stress and strain are converted from the test and FE force and displacement results by dividing the displacement by the height of the unit cell and the load by the cross-sectional area of the unit cell, respectively. The height of the assembled single unit cell is ≈64 mm, and the cross-sectional area could be obtained by dividing the cell's height from the total volume of the unit cell.

The compression test results in Figure 10 exhibit an overall near-linear increase in load with deformation, punctuated by fluctuations that can be attributed to the variability and small-scale unevenness of the as-printed friction surfaces in the FDM-fabricated unit cells. Upon initiation of the unloading step, the force rapidly decreases to a relatively small value. However, as the displacement continues to decrease, in several cases this force experiences a slight rebound, remaining at a similar level until the displacement reaches zero. In others, there is a pronounced inflexion in the curve, with this force gradually returning to zero. The FE simulation with a COF value of 0.547, the same value as the COF measured in the experiment, exhibits a qualitatively similar pattern, with a rapid drop in vertical reaction as compression is released, followed by a slight rebound and then stabilization. No permanent deformation was observed during the compression tests, but sometimes the unit cell had to be manually reset to its original position when the restoring force from the frame became insufficient to overcome the effects of stiction between the 3D printed contact surfaces near the end of the load cycle.

The energy dissipated during each compression cycle is obtained by calculating the difference between the energy accumulated by the structure during loading and that released during the unloading part of the cycle, that is, the area enclosed by the loading and unloading curves in Figure 10 and the force–displacement graphs in Figure S3 (Appendix SC, Supporting Information). The energy dissipation predicted by the theoretical model and the FE simulations is compared to the experimental measurements in **Figure 11**, which includes error bars to illustrate the range of variation in the experimental results.

The actual values of the energy dissipation per compression cycle for both conventional and re-entrant unit cells are summarized in Table 2.

It is clear that the energy dissipation performance of the unit cells with re-entrant frames (Figure 3b) was better on average than that of those unit cells with conventional hexagonal frames (Figure 3a). However, this difference in dissipation tended to decrease as the displacement and consequently the effective strain increased. While for a 1 mm maximum compression the average energy dissipation from three separate experiments measures 59.5 mJ for the traditional hexagonal model and just over 71 mJ for the re-entrant structure, which represents an improvement of 19%, when the maximum compression is increased to 2 mm, the difference in favor of the re-entrant hexagon frame decreases to ≈10%. And when the maximum compression reaches 3 mm, the range of energy dissipation values obtained from the experiments is similar for both, so it is not clear whether a difference persists. The FE simulation results mirrored this difference between the unit cells with conventional and re-entrant hexagonal frames, but it clearly persisted as the compression increased.

The equivalent (Von-Mises) stress distribution over the model geometry in the FE simulations is also investigated, and in the 13-unit cell geometry case, the equivalent stress distribution of the cells located at the edges of the middle layer was smaller than the stress distribution of the cells located at the top or bottom layer (Figure S5, Supporting Information). This is due to the fact that this 13-unit cell geometry was assumed to be in the middle of a structure consisting of a myriad of unit cells and set boundary conditions so that the same displacement occurs on the outer faces located at the same height.

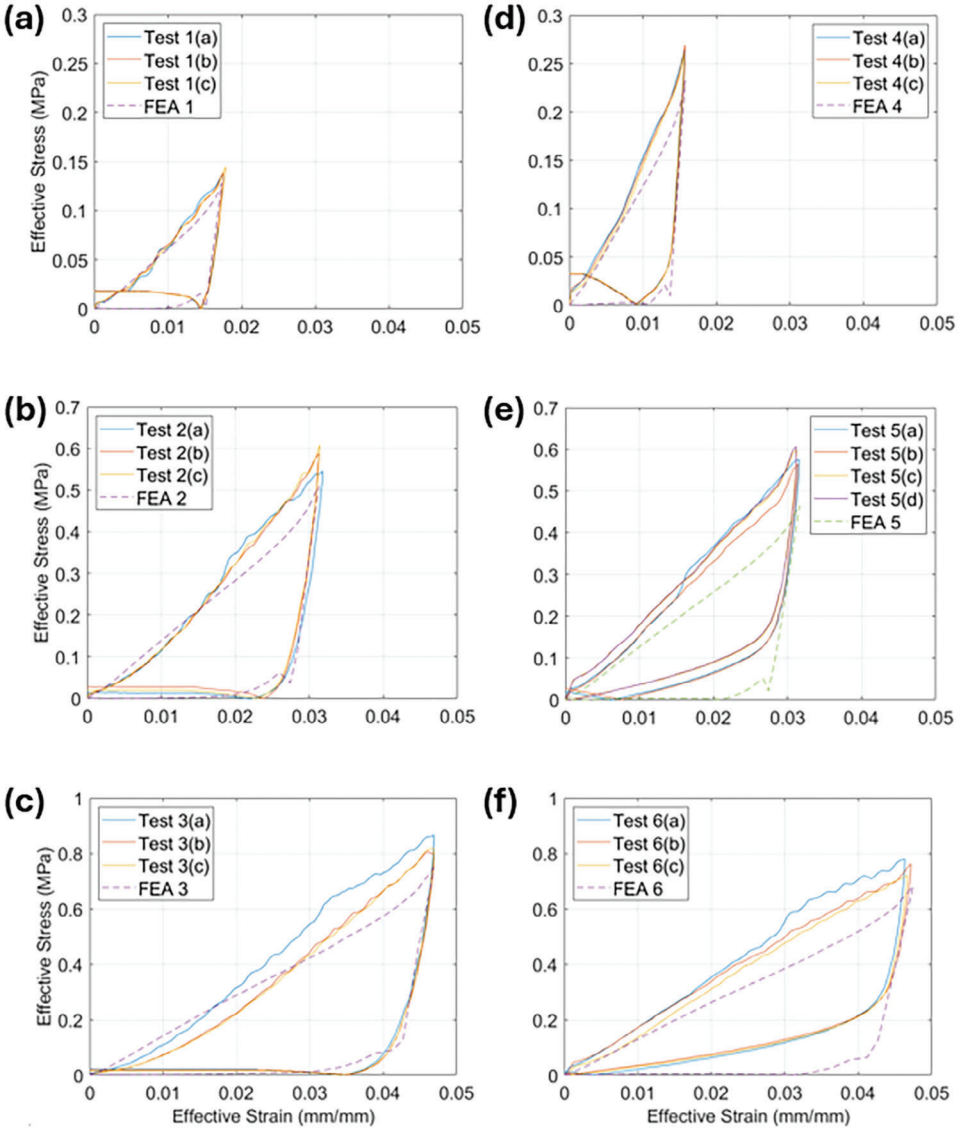

Figure 10. Effective stress-strain results from compression tests and FE simulations for (a) 1 mm displacement cycle (1.56% maximum strain), (b) 2 mm displacement cycle (3.1% maximum strain) and (c) 3 mm displacement cycle (4.67% maximum strain) applied to a unit cell with a conventional hexagonal frame; and equivalent results for (d) 1 mm displacement cycle, (e) 2 mm displacement cycle and (f) 3 mm displacement cycle applied to a unit cell with a re-entrant hexagonal frame.

The FE simulation results for a single unit cell and three finite metamaterials constructed from different numbers of the same unit cell are presented in **Figure** 12a. Note that when calculating the effective strain for the multi-unit cell models the maximum height of the structure (the height of the odd columns of multi-unit cell models) is used instead of the average height to get a consistent maximum effective strain value for each simulation. It can be observed that the height of the cycles, that is, the reaction force to a given compression, varies with the number of unit cells and the height to width ratio of the assembled structure but its overall shape of the load remains relatively consistent as evidenced by their total energy dissipation performance.

The resulting energy dissipation per unit volume during each compression cycle is plotted in Figure 12b, which illustrates a clear trend from the single cell through the 8-unit system to the 11-unit and 13-unit cells models. The actual values computed from the simulations are 1.8282×10^{-4}, 1.5258×10^{-4}, 1.4814×10^{-4} and 1.4837×10^{-4} mJ mm^{-3} respectively, representing a 20% decrease from the single unit cell when the number of unit cells exceeded 10.

The results of the simulations of a metamaterial with many unit cells, as represented by an RVE with PBC, are presented in **Figure** 13, along with the corresponding results for a single hexagonal unit cell without PBC, in order to study the influence of PBC. Figure 13a,b is contour plots that visually depict the distribution of stress when compressed by 3 mm, consisting of 1.5 mm in the negative y-axis direction on the top face and 1.5 mm in the positive y-axis direction on the bottom face, in

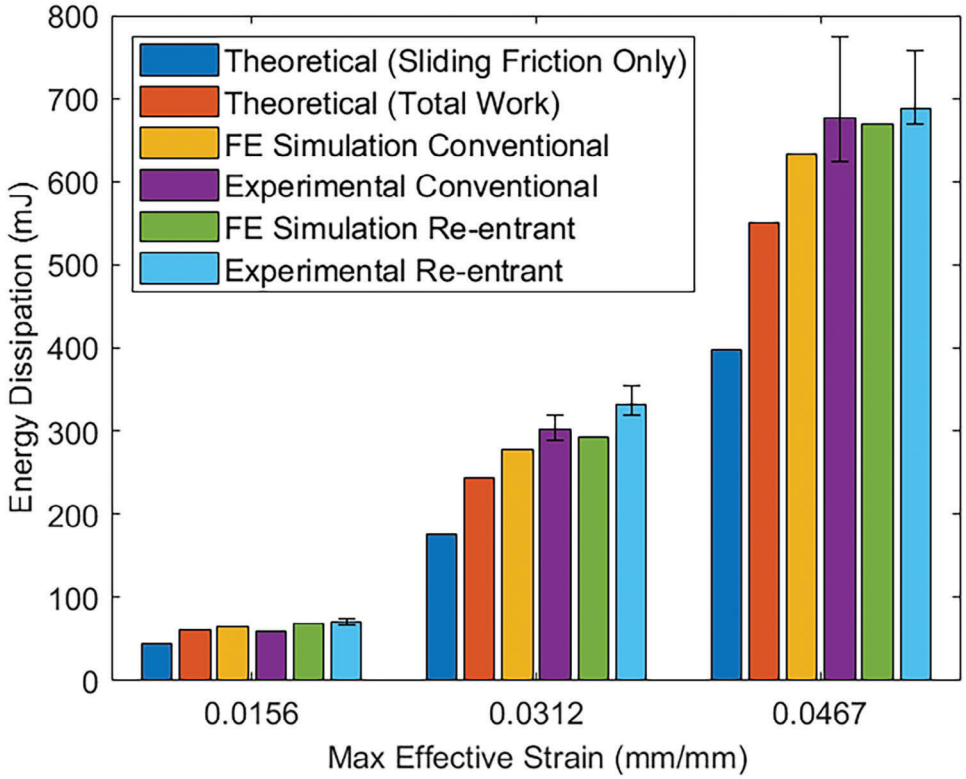

Figure 11. The energy dissipation per compression cycle was calculated from the theoretical model, the FE simulations, and the experimental data, with error bars for the experiments; and the total energy absorbed during the loading phase of the cycle as calculated from the theoretical model.

both models. A scale factor of 3.6 is used to make the deformed geometry more clearly visible. FE simulation results reveal that the equivalent stress distributions of the two oblique sides of each model under the same y-directional uniaxial displacement conditions are significantly different. In the RVE cell the oblique sides experience higher stress compared to the single hexagonal unit cell without constraint equations, resulting in a difference in deformation with respect to the center hexagonal frame. The higher stress cause in-plane bending at the lower part of the oblique sides, and out-of-plane bending deformation at the upper part of the oblique walls, as shown in Figure 13a. The hysteresis loops of the RVE cell and the single hexagonal unit cell in the FE simulation are plotted in Figure 13c, where the paths of the force–displacement curves are substantially divergent due to the varying degree of bending. The peak force value at the end of loading step is about two times higher for the RVE cell than for the single unit cell, and the energy dissipation is ≈40% higher.

4. Discussion

Aside from the well-known variability of 3D printed part shapes and dimensions relative to computer-aided design model geometry, the disparities between the results from compression experiments and FE simulations can be attributed to two main factors. The first is the reliance of FE simulations on idealizations, particularly around contact and friction at the interface between the blades and the columns but also in connections. For example, the connection between the hexagonal frame and the connecting upper and lower parts were modeled as perfectly bonded. However, the actual fabricated parts were assembled using interference fits, which may not be as rigid.

The other and perhaps more important factor is that simulated material properties do not perfectly match real-world behavior. The unit cell FE simulations used the CPE HG100 compressive modulus as measured by 'American Society for Testing and Materials' standard tests. However, because parts of the unit cell structure such as the frame are acting in bending and the measured tensile modulus is significantly higher than the compressive one, the real unit cells can be expected to be stiffer than in the simulation.

For the unit cell with the conventional hexagonal frame, Figure 10 shows good qualitative agreement between the shapes of the experimental and computational compression cycles. The experiments consistently produced a higher peak load during loading and slightly higher load during the inflection of the unloading curve, which is consistent with the expectation of the experimental unit cell being stiffer due to the material being significantly stiffer in tension and bending than in compression. For the re-entrant frame the differences are more marked, with experimentally measured loads being noticeably higher than those predicted by the simulations, particularly for higher compressions. This is because the re-entrant geometry induces higher bending of the frame corners, increasing the influence of the difference between the material's tensile and compressive moduli. There is also less rebounding during unloading which is interpreted as the manufactured re-entrant frame storing greater elastic energy

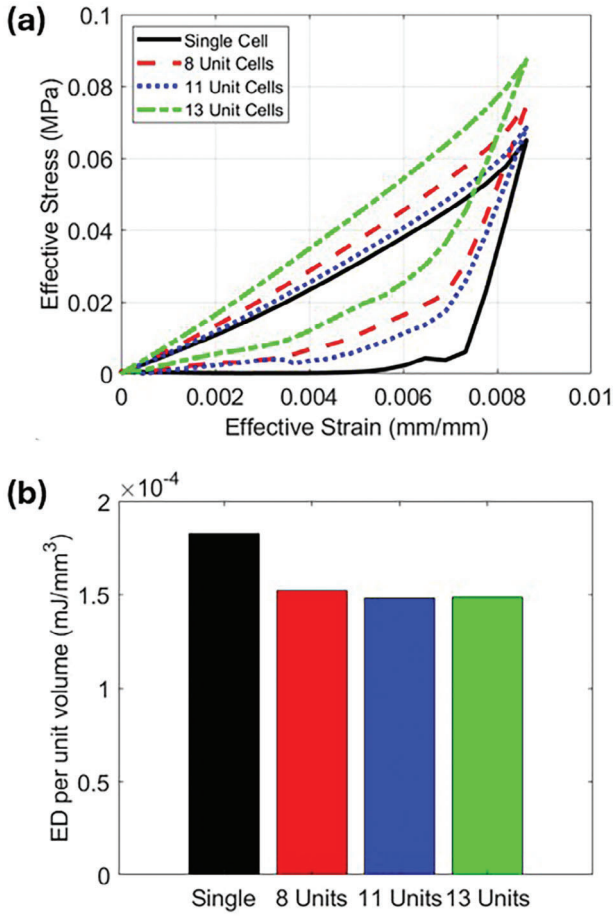

Figure 12. (a) Effective stress–effective strain curves from FE simulations of the single unit cell under a 0.5 mm compression cycle, the 8-unit and 13- unit cell metamaterials under a 1.5 mm compression cycle, and the 11-unit cell metamaterial under a 2 mm compression cycle; and (b) the energy dissipation per unit volume calculated from the FE simulations for these compression cycles.

during loading than predicted and facilitating positive separation of the contact surfaces due to the negative Poisson's ratio effect upon unloading.

The single unit cell FE simulation results below the inflection point of the unloading step show a gradual decrease toward zero, unlike the plateaus in the experimental data. In practical experiments, it was observed that in most cases, the load reaches zero before the end of the unloading step, after which it either increases until the end of the unloading step or reaches a certain level and stabilizes. This discrepancy between experiments and simulations is hypothesized to stem from the fact that, unlike the simulation model under ideal boundary conditions, in the physical model the contact surfaces, with their aforementioned small-scale unevenness, are not positively separated during the unloading process. The irregular contact surfaces lead to high stick-slip during the loading process, preventing them from completely returning to their original non-contacting state. During the loading step of experiments, significant internal stresses are developed within the contact interfaces due to frictional forces and deformation. The observed rebound in force after it reduces to zero in the unloading step is indicative of these residual internal stresses. As the external load is removed, the internal stresses attempt to restore the structure to its original configuration. However, due to the frictional locking and micro-scale interactions, the columns do not fully return to a stress-free state. This leads to a bounce back to positive force as the internal stresses are partially released. After the initial rebound, the force stabilizes to a constant positive value during the remainder of the unloading step. This constant force represents the equilibrium state where the residual internal stresses are balanced by the frictional forces at the contact interfaces. The micro-scale roughness and asperities at the contact surfaces prevent complete separation, resulting in a persistent contact force even in the absence of an external load. On the other hand, in the FE simulation, ideal boundary conditions and smooth contact surface geometries are assumed, which do not fully capture the complex microscale interactions and frictional behavior observed in the physical model. Consequently, the simulation shows a more idealized unloading response, where the force decreases back to zero after the rebound, as the model does not account for the residual internal stresses and persistent frictional forces present in the actual experiment.

The energy dissipation calculated from the theoretical model, from frictional sliding only, was found to be only about two-thirds of the energy dissipation measured from the experimental and simulation models across all displacements. However, adding all three components of work (Equation 17) resulted in better alignment with the experiments. The discrepancy between the theoretical model and the other models is due to the oversimplification of the theoretical model, which results in the theoretical model's estimate of the normal force on the contact surface being significantly off, and also to the uneven nature of the additively manufactured contact surface and the practical difficulties in accurately capturing the resulting frictional forces across the sliding surfaces. While the FE simulation predictions are better, generally being in the neighborhood of the lower end of the range of experimentally derived values and ≈10% lower than the experimental average for the 3 mm compression cycle. The FE simulations also match the experimental observations in that the energy dissipation calculated for the unit cell with re-entrant frame is higher than for the conventional frame for all compression cycle depths. However, since the 55×10^3 mm^3 volume of the re-entrant unit cell is ≈12.4% greater than that of the 49×10^3 mm^3 conventional unit cell, the actual energy dissipation per unit volume of the conventional hexagonal unit cell is higher than that of the re-entrant version. For the deepest compression cycle this energy dissipation density reaches 0.0143 mJ mm^{-3} (average experimental) or 0.0129 mJ mm^{-3} (FE simulation) for the conventional unit cell versus 0.0126 mJ mm^{-3} (average experimental) or 0.0122 mJ mm^{-3} (FE simulation) for the re-entrant version.

As more unit cells are added to the FE model, the peak compressive force and effective stress tended to be larger, while the values of energy dissipation per unit volume tended to be smaller. For example, the 8- and 13-unit cell models had 14.9% and 34.5% higher peak stress, respectively, compared to the single-unit cell model. However, the energy dissipation per unit volume was 19.8% and 23.2% lower than that of single unit cell, respectively, which is due to the nature of having a sliding friction surface inside the unit cell, where the honeycomb structures in each half of

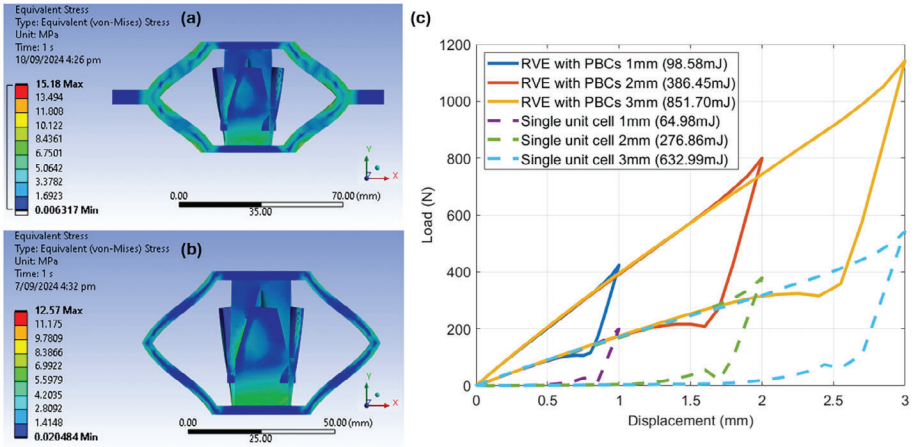

Figure 13. Comparison of the visualized deformation aspects and the numerical discrepancies in terms of equivalent stress and energy dissipation. a) Equivalent stress distribution in the RVE geometry with PBCs applied and a displacement of 1.5 mm on the top and bottom faces, respectively, facing each other toward the center which equal to the totally 3 mm displacement. b) Equivalent stress distribution in the single conventional hexagon unit cell without PBCs and a displacement of 1.5 mm on the top and bottom faces, respectively, facing each other toward the center. c) Force–displacement plots were obtained from FE simulation by using RVE model with PBCs and single conventional unit cell without PBCs.

the top and bottom of the even-numbered columns are inevitably excluded from the sliding mechanism, with or without the geometry inside the hexagonal structure. It is interesting to note that while the energy dissipation per unit volume for the 11-unit cell models is close to that of the 13-unit cell, the peak efficient stress is ≈9% lower than even that of the 8-unit cell, suggesting that the addition of more rows of unit cells toward the axis where an external force is applied, can lead to results similar to the peak efficient stress value of the single unit cell. The middle units of an even row will exhibit a sliding mechanism indirectly in response to its neighboring cells, unlike the odd rows where the displacement condition is set directly at the top. As a result, it seems reasonable that the energy dissipation per unit volume values for metamaterial models with a limited number of unit cells tend to decrease as the number of even-numbered columns increases. However, assuming a frictional metamaterial with an infinite number of honeycomb structures, especially with many rows, it can be inferred that the proportion of half-unit cells that are excluded from the energy dissipation mechanism at both ends of the metamaterial will be infinitesimally small in the total metamaterial, and in this case, the results will be almost identical to those of the single cell model.

The higher stresses in the RVE cell with PBCs significantly affects the path of the force–displacement curves. The change in the peak force at the maximum displacement between the RVE cell and single hexagonal unit cell is approximately double, an increase which can be interpreted as a consequence of the additional stiffness induced by the PBC constraints in the RVE cell. In terms of energy dissipation, the RVE cell achieves a higher quantity of ≈40%, due to an increase in the frictional stress levels during contact and sliding between the columns and blades. In other words, this result reveals that the proposed frictional metamaterial will have significantly better energy dissipation performance than a single unit cell and holds promise for applications requiring repeatable energy dissipation under relatively slow to moderate loading rates, that is, vibration damping and not impact or shock.

In future work, energy dissipation improvements were explored by applying various patterns on the contact surfaces within the current metamaterial concept. Additionally, considering the diversity of 3D printing methods (e.g., FDM, Selective Laser Sintering, Stereolithography), the investigation was focused on how these methods affect energy dissipation. While this study utilized FDM due to accessibility, a future research avenue involves comparing energy dissipation across various additive manufacturing methods. In addition, the proposed theoretical model has difficulties in accurately capturing the energy dissipation of these frictional metamaterials, so future work will explore ways to improve this model.

5. Conclusion

This paper proposes a mechanical metamaterial that dissipates energy through friction while operating within the elastic regime, which allows it to perform repeated energy dissipation cycles, unlike many other mechanical metamaterials and architected materials that depend on plasticity and fracture. It also differs from other metamaterials that use friction in the novel design of its frictional mechanism. The proposed frictional metamaterial was studied through experiments, theoretical analysis, and FE simulations of its unit cell. Both conventional and re-entrant versions of the hexagonal unit cell were considered. For the experiments, multiple unit cells were manufactured by 3D printing with CPE HG100, a stiff polymer. Once the computational simulation had been validated through comparisons to the experimental data and theoretical model, it was then extended to the simulation of finite meta-material specimens consisting of less than and more than ten-unit cells.

When the unit cells were subjected to low-speed compression cycles there was a good match between the shapes of the experimental and computational load–displacement curves. However, the experimental curves exhibited higher force and stress for any given displacement than those produced by the FE model, that is, the curves were shifted up. This difference was relatively minor

for the conventional hexagonal unit cells but more marked for the re-entrant cells, and this greater stiffness of the physical unit cells was attributed to the use of the compressive elastic moduli in the simulations.

This similarity between the shapes of the load–displacement curves expressed itself in good agreement between experiments and simulations in the area between the loading and unloading curves, and therefore the energy dissipated per cycle, particularly for the conventional hexagonal unit cell. When the FE simulations were extended to finite metamaterials, it was found that with the change in unit cell boundary conditions, there was a drop-in energy dissipation per unit cell, but this reduction tapered off once there were more than ten-unit cells in the metamaterial.

These results demonstrate the potential of this frictional metamaterial concept to provide superior elastic energy absorption and dissipation performance. This makes it an interesting solution for applications in which repeated energy dissipation or damping under cyclical loads is required in combination with light weight. Future unit simulations and experiments on unit cells using different constituent materials and additive manufacturing methods will explore the potential of different combinations, and the influence of varied loading rates.

Supporting Information

Supporting Information is available from the Wiley Online Library or from the author.

Conflict of Interest

The authors declare no conflict of interest.

Data Availability Statement

The data that support the findings of this study are available from the corresponding author upon reasonable request.

Keywords

elastic energy dissipation, frictional metamaterial, hexagonal and re-entrant unit cells

Received: April 18, 2024
Revised: September 19, 2024
Published online: October 30, 2024

[1] I. O. Lopez, J. M. Busturiab, H. Nijmeijera, *J. Sound Vibration* **2004**, *278*, 539.
[2] N. Meyer, R. Seifried, *Nonlinear Dyn.* **2022**, *108*, 3009.
[3] H. Yang, L. Ma, *Mater. Des.* **2020**, *188*, 108430.
[4] E. Giuriani, A. Marini, *Int. J. Archi. Heritage* **2008**, *2*, 226.
[5] C. Yenidogan, *Vibration* **2021**, *4*, 602.
[6] V. Crupi, E. Kara, G. Epasto, E. Guglielmino, H. Aykul, *Int. J. Impact Eng.* **2015**, *77*, 97.
[7] R. Jiang, Z. Gu, T. Zhang, D. Liu, H. Sun, Z. Pan, D. Peng, *Aerospace* **2021**, *8*, 279.
[8] V. Khatkar, B. K. Behera, *Adv. Compos. Mater.* **2020**, *29*, 129.
[9] N. S. Ha, V. T. Le, N. S. Goo, *J. Bionic Eng.* **2018**, *15*, 57.
[10] N. Lee, M. F. Horstemeyer, H. Rhee, B. Nabors, J. Liao, L. N. Williams, *J. R. Soc., Interface* **2014**, *11*, 20140274.
[11] S. Fischer, M. Thielen, R. R. Loprang, R. Seidel, C. Fleck, T. Speck, A. Bührig-Polaczek, *Adv. Eng. Mater.* **2010**, *12*, B658.
[12] C. W. Hull, *Res.-Technol. Manag.* **2015**, *58*, 25.
[13] S. Zhu, X. Zhang, *National Sci. Rev.* **2018**, *5*, 131.
[14] L. Mizzi, K. M. Azzopardi, D. Attard, J. N. Grima, R. Gatt, *Phys. Status Solidi RRL* **2015**, *9*, 425.
[15] Z. Wang, C. Luan, G. Liao, J. Liu, X. Yao, J. Fu, *Adv. Eng. Mater.* **2020**, *22*, 2000312.
[16] W. Cai, U. K. Chettiar, A. V. Kildishev, V. M. Shalaev, *Nat. Photonics* **2007**, *1*, 224.
[17] D. Schurig, J. J. Mock, B. Justice, S. A. Cummer, J. B. Pendry, A. F. Starr, D. R. Smith, *Science* **2006**, *314*, 977.
[18] C. Yuan, X. Mu, C. K. Dunn, J. Haidar, T. Wang, H. J. Qi, *Adv. Funct. Mater.* **2018**, *28*, 1705727.
[19] R. Kumar, M. Kumar, J. S. Chohan, S. Kumar, *Mater. Today: Proc.* **2022**, *56*, 3016.
[20] V. G. Veselago, *Soviet Physics Uspekhi* **1968**, *10*, 509.
[21] J. B. Pendry, A. J. Holden, D. J. Robbins, W. Stewart, *IEEE Trans. Microwave Theory Tech.* **1999**, *47*, 2075.
[22] U. Leonhardt, *Science* **2006**, *312*, 1777.
[23] R. Xue, X. Cui, P. Zhang, K. Liu, Y. Li, W. Wu, H. Liao, *Extreme Mechan. Lett.* **2020**, *40*, 100918.
[24] Y. S. Hamidreza, A. H. Akbarzadeh, A. Mirbolghasemi, K. Hermenean, *Mater. Des.* **2018**, *160*, 179.
[25] Z. Zhai, L. Wu, H. Jiang, *Appl. Phys. Rev.* **2021**, *8*, 041319.
[26] K. Fu, Z. Zhao, L. Jin, *Adv. Funct. Mater.* **2019**, *29*, 1901258.
[27] A. P. Garland, K. M. Adstedt, Z. J. Casias, B. C. White, W. M. Mook, B. Kaehr, B. H. Jared, B. T. Lester, N. S. Leathe, E. Schwaller, B. L. Boyce, *Extreme Mech. Lett.* **2020**, *40*, 100847.
[28] T. R. Giri, R. Mailen, *Int. J. Mech. Sci.* **2021**, *204*, 106541.
[29] J. Li, Z. Chen, Q. Li, L. Jin, Z. Zhao, *Adv. Sci.* **2022**, *9*, 2105769.
[30] A. Bacigalupo, V. Diana, L. Gambarotta, *Int. J. Solids Struct.* **2023**, *273*, 112213.
[31] C. Mercer, T. Speck, J. Lee, D. S. Balint, M. Thielen, *Int. J. Impact Eng.* **2022**, *169*, 104315.
[32] C. B. Morris, L. Bekker, C. M. Spadaccini, M. R. Haberman, C. C. Seepersad, *Adv. Eng. Mater.* **2019**, *21*, 1900163.
[33] S. J. Ling, J. Sanny, W. Moebs, *University Physics.*, OpenStax, Rice University **2016**.
[34] L. J. Gibson, *MRS Bull.* **2003**, *28*, 270.
[35] R. G. Budynas, A. M. Sadegh, *Roark's Formulas for Stress and Strain, 9E*, McGraw Hill LLC, New York City **2020**.
[36] F. P. Beer, E. R. Johnston, J. T. DeWolf, D. F. Mazurek, *Mechanics of Materials*, McGraw-Hill Education, New York City **2015**.